Variable Stiffness Soft Robotic Fingers using Snap-Fit Kinematic Reconfiguration

Jérôme Bastien, Lionel Birglen, *Senior Member, IEEE,*

***Abstract*—Versatile and secure grasping in robotic systems remains a difficult challenge to address when objects possess a wide range of different properties (size, weight, friction coefficient, etc.). The human hand is often the primary source of inspiration for many technologies addressing this challenge and a notable feature of our hands is that they can vary their stiffness to match the requirements of the task, e.g. become stiffer or more compliant depending on specific requirements. Many robotic devices have been proposed in the literature mirroring this capability, either using an adjustable internal tension mechanism similar to what happens with human tendons or another physical phenomenon yielding the same effect. This paper proposes a new type of soft robotic fingers using a novel method to produce a variable stiffness achieved by modifying the kinematic structure of the fingers using snap-fit joints, a very simple alternative to most variable stiffness mechanisms. The resulting modification of the geometry and kinematics of the fingers, including their number of degrees of freedom, allows to greatly alter the intrinsic stiffness of the grasp produced by these fingers. A notable feature of the proposed new design is that one pair of fingers can be used to switch the stiffness of another pair if a dual arm robot is used.**

***Index Terms*—Grasping, Soft Robot Applications, Compliant Mechanisms, Variable Stiffness**

I. Introduction

GRASPING objects of various geometries and material properties has been and still is a lasting and difficult challenge for robotic manipulators. Securing seized objects that are very different both in terms of shapes or textures calls for a versatile grasper capable of gently enveloping these objects and providing both form- and force-closure but also not exerting an excessive contact pressure that could lead to damages [1]. In practical industrial robotics, the most commonly used grippers are simple two- or three-finger tools, often pneumatically driven, with high stiffnesses [2]. Nevertheless, simple industrial grippers are also often unsuitable for more delicate operations where the objects they must seize are fragile, and their use is a concern in human-robot interactions. To address these issues, compliant or soft grippers have been proposed and define a novel category of robotic grippers. These soft grippers have a low intrinsic stiffness which can be taken advantage of both to provide an enveloping motion for the seized objects [3] but also to mitigate or completely eliminate potential harmful interactions with a human during a collision. Another secondary advantage of soft grippers is that they are often significantly less expensive and lighter than their rigid counterparts [4], [5]. On the other hand, soft tools are generally weaker and far less precise. A handful of soft grippers are now commercially available such as the ones from Soft Robotics Inc., Ubiros, OnRobot, The Gripper Company, or Festo with the Fin Ray Effect (FRE) fingers [6], [7]. The latter, illustrated in Fig. 1, have the distinctive particularity of providing shape-adaptation while being completely passive, i.e. they do not embed any actuator but instead rely on the motion of the gripper to which they are attached to provide the required closing and opening motions.

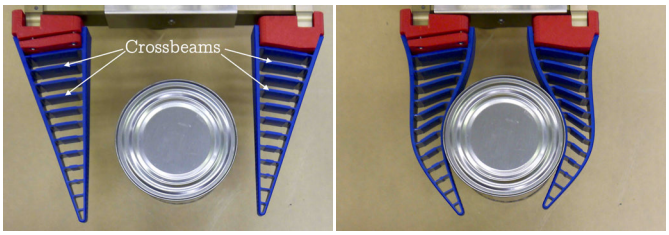

(a) Open (b) Close

Fig. 1. Example of the closing motion of a FRE finger by Festo attached to a pneumatic gripper

To strike a balance between safety, versatility, and load capability is challenging and new designs of soft grippers are still currently revealed to this aim [8]–[11]. An interesting avenue proposed in the literature to solve these conflicting requirements is to dynamically change the stiffness of soft grippers. A soft gripper with variable stiffness can change from a stiff mode where it is capable of producing large forces and provide a greater positional accuracy to a compliant mode where it can gently envelop objects and is safe in case of collision. Different solutions to produce a variable stiffness of soft tools or robot joints have been proposed, e.g. in [12]–[15]. Theses solutions can be broadly sorted out in two categories: designs that achieve variable stiffness electronically, i.e. with a proper control algorithm [16], and these achieving this effect by mechanical means, i.e. through a physical variation in the property of the device.

Among mechanical solutions, ”bulk locking” is commonly found and used with grippers composed of small-sized particles enclosed in a soft shell [17], [18]. This bulk locking is produced by changing the interactions of the

École Polytechnique de Montréal, Montréal, Québec, H3C 3A7, Canada, email: jerome.bastien@polymtl.ca

Manuscript received xxx; revised xxx.

IEEE Transactions on Robotics (T-RO) paper, presented at ICRA 2024, Yokohama, Japan. Cite as T-RO paper.

embedded particles either by applying a magnetic field [19] or by reducing the pressure inside the shell which greatly stiffens the gripper. Another solution to achieve a variable stiffness mechanism is through the use of low melting alloy material [20], [21] allowing to change from a very stiff solid state to a soft liquid one, resulting in a dramatic drop in stiffness. A third approach yet to yield variable stiffness is to rely on inertial properties, for instance in [22] the cross-sections (and thus, second moment of inertia) of the flexure hinges in a finger are changed by a secondary actuator. Similarly, the compliant fingers with lattice structure proposed by [23] can change their stiffness with the rotation of internal wheels. Another technique, still sharing a similar approach, was introduced in [24] where the internal structure of a flexure inside robotic arm changed to make it more or less flexible depending on its speed in order to absorb shocks and reduce the risk of injury to surrounding humans during movement. A final example of variable stiffness mechanisms using the mechanical approach is [25], where compliant prismatic and revolute joints are shown that can achieve two dramatically different states of stiffness using a secondary statically balancing linkage applied to the joint.

II. Kinematic and Position Analyses

A. Introduction

The fingers proposed in this paper are inspired by the FRE fingers shown in Fig. 1. In the embodiment presented in that figure, the fingers are composed of 12 internal crossbeams with living hinges connecting the flexible front and back surfaces of the finger. In a previous work by one of the authors [26], it was shown that the number and stiffness of these crossbeams have a considerable influence on the contact forces produced by the fingers and thus, their stiffness. In its most simplistic realization, a FRE finger could have no crossbeam at all and such embodiment, conceptually shown in Fig. 2e would generate weak contact forces, i.e. the softest finger for a constant front and back surfaces. Adding as few as a single crossbeam, which acts as a stiffener for the finger, greatly increases stiffness as will be demonstrated. However, the actual geometry of this crossbeam and especially the position where it is connected to the finger also has an impact on the resulting forces. By discretizing the front and back surfaces of the finger into three rigid links connected by flexures, four connecting combinations are found, see Figs. 2a-2d. By convention, in all figures showing the schematic of a finger in this paper, the front side of the finger (intended for contacting objects) is on the left (points O, A, B) and the back of the finger is on the right (points F, E, D), unless otherwise specified. The links closest to the base are referred to as proximal, while these that are the farthest from the base are the distal links. Between the proximal and distal links on each side one finds the intermediate front and back links, see Fig. 3. Front links are also referred to as phalanges since their are meant for contacting objects. To distinguish between the four design variants illustrated in Fig. 2, they are all designated with a unique shorthand notation as shown in the figure captions. These five fingers have very different kinematic structures as can one plainly see. The prismatic joint at the base the fingers stands for the actuating gripper they are attached to.

The main objective of the kinematic analysis of the fingers is to establish the force-displacement relationships they produce in order to determine their stiffness. These relationships can be obtained by calculating the forces required to maintain static equilibrium for a known configuration (angles between the links) and the most convenient method to compute these forces is by means of establishing the virtual work of each finger [27]. In order to obtain this virtual work, the first step is to establish the kinematic coefficients relating the angular rate in all joints where a torque is acting as functions of the selected degrees of freedom (DOF). In our case, the fingers being soft, all revolute joints of the pseudo-rigid body models depicted in Fig. 2 have an acting elastic torque. It is worth noting that the accurate computation of the contact forces produced by soft fingers is a challenging issue and most of the available literature focuses on deformation modeling. Contact forces are generally obtained through FEA and although this method indeed leads to very accurate results it is very computationally intensive and thus, not ideal for design optimization. Using a virtual work approach to compute grasp forces of soft fingers as proposed in this work has only been previously introduced in a single work [26] and as will be shown, also leads to very accurate results for the fingers considered here. The accurate and fast computation of the grasp forces produced is essential for the optimization of the soft fingers with a robust algorithm simulating thousands of designs and grasps as discussed in Section V.

Fig. 3 depicts the general geometry and nomenclature of the fingers introduced in Fig. 2. A reference frame is attached to each finger at point O and the $\mathbf{x}$-axis of this frame is aligned with the direction of the prismatic joint driving the finger. The relative angles between the front (F) and back (B) links of the fingers are θ_i^F $(i = 1, 2, 3, 4)$ and θ_i^B $(i = 1, 2, 3)$ respectively. The contact forces between the finger and the object are assumed normal to the link where they occur and of magnitudes f_i $(i = 1, 2, 3, 4)$. Note that the f_4 contact force introduced in Fig. 3 exists to statically constrain the finger but is not used during normal operations as will be discussed. The force $\mathbf{f}_a$ at the base of the fingers corresponds to the linear actuation moving the finger in translation toward the objects, i.e. the gripper to which the fingers are attached. The position of a contact force of magnitude f_i along its phalanx is measured by d_i. Throughout the paper, $\mathbf{r}_{XY}$ will be used to refer to the vector going from point X to point Y and l_{XY} is the norm of that vector. For instance, $\mathbf{r}_{OA}$ is the vector from O to A, i.e. along the contact surface of the proximal phalanx, and $l_{OA} = \|\mathbf{r}_{OA}\|$ is the length of this phalanx. A few lengths that will be used often in the paper are designated by a shorthand notation, namely: $l_0 = l_{OF}$, $l_1 = l_{OA} = l_{FE}$, $l_2 = l_{AB} = l_{ED}$, $l_3 = l_{BC} = l_{DC}$, see Fig. 3. All lengths are constant for a specific design of a finger. As the proximal and intermediate links are ternary by nature, potentially connecting a crossbeam, the vectors $\boldsymbol{\epsilon}_i^F$ and $\boldsymbol{\epsilon}_i^B$ are used to parameterize the location of these potential attachment points and they are

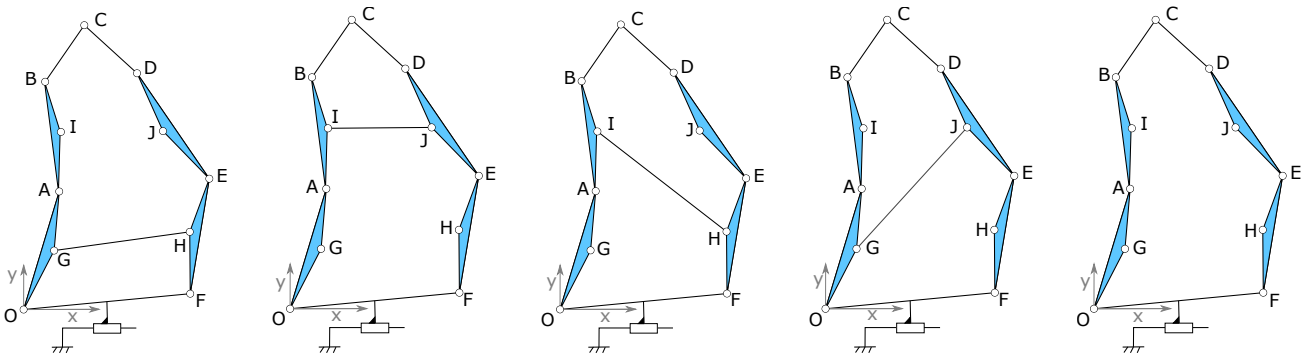

(a) 1L (b) 2L (c) 1R (d) 2R (e) W

Fig. 2. Pseudo-rigid design of FRE fingers with a single (a-d) or no (e) crossbeam

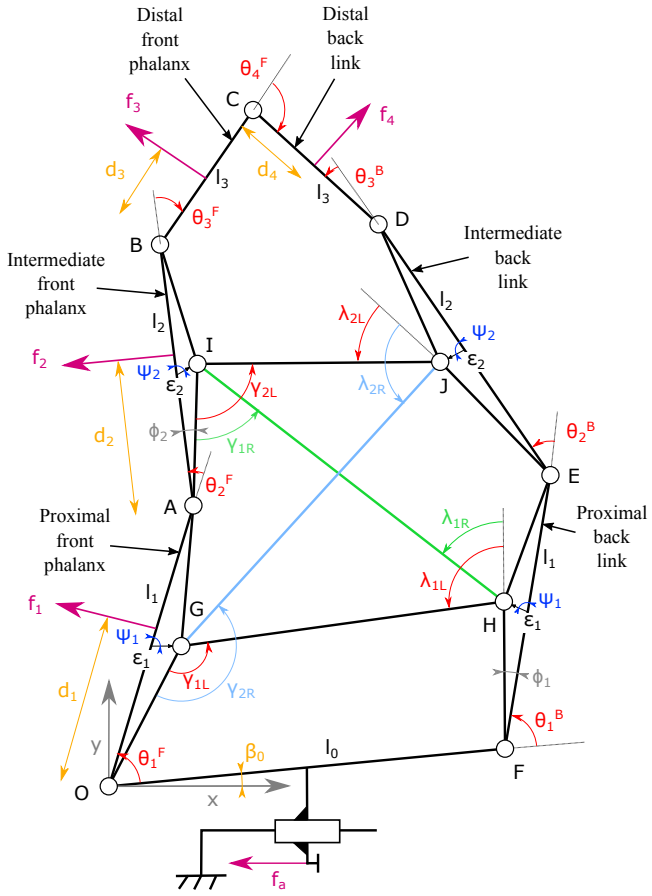

Fig. 3. Geometrical parameters of the fingers

defined as going from the middle of the i^{th} link to the nearest crossbeam joint on the same link. Keeping the symmetry of the fingers, is is assumed that:

$$\|\boldsymbol{\epsilon}_1^F\| = \|\boldsymbol{\epsilon}_1^B\| = \epsilon_1 \quad \text{and} \quad \|\boldsymbol{\epsilon}_2^F\| = \|\boldsymbol{\epsilon}_2^B\| = \epsilon_2. \tag{1}$$

The angle between $\boldsymbol{\epsilon}_i$ and the associated front or back link is noted ψ_i, see Fig. 3, and is a constant as well as angle ϕ_i. Other angles γ_X and λ_X are also defined in the figure and correspond to the angles between the internal crossbeam of finger X and its attachment link on the front and back side respectively. Conversely to ψ_i and ϕ_i, angles θ_X, γ_X and λ_X are variable and depend on the configuration of the finger.

Once the geometry of the fingers is completely parameterized, the first step to compute the virtual work of the fingers is to determine the number of DOF for each finger. This number actually depends on which version of the finger is considered and can be computed using textbook formulae, e.g. [28]. One can then establish that the first four fingers shown in Fig. 2 have three DOF while type W has four. This increased DOF is the reason why a fourth contact force apparently occurring at the back of the finger is depicted in Fig. 3. As will be shown later in the paper, this seemingly nonsensical contact force does not impact the optimization of the finger and the objective of producing a variable stiffness design. The only usefulness of this fourth force is to make the subsequent equations consistent between fingers.

B. Velocity Equations

Once the number of DOF for the different fingers is known, the second step is to determine the overall velocity equations relating the angles selected as the DOF to all the other angles in the linkage in order to be able to compute the overall virtual work of the linkage. The choice of which variables are DOF is arbitrary and in this work the front phalanx angles were selected. With the version W finger, a fourth angle θ_4^F is added as shown in Fig. 3. For three-DOF fingers, the velocity equation of the linkage has the following form:

$$\mathbf{A}_X \begin{bmatrix} \dot{\theta}_1^B \\ \dot{\theta}_2^B \\ \dot{\theta}_3^B \\ \dot{\theta}_4^F \\ \dot{\gamma}_X \\ \dot{\lambda}_X \end{bmatrix} = \mathbf{V}_X \begin{bmatrix} \dot{\theta}_1^F \\ \dot{\theta}_2^F \\ \dot{\theta}_3^F \end{bmatrix}. \tag{2}$$

with $X \in \{1L, 2L, 1R, 2R\}$. Matrices $\mathbf{A}_X$ and $\mathbf{V}_X$ are of dimensions 6×6 and 6×3 respectively and can be obtained by differentiating kinematic vector closure equations [26]. These equations are obtained by equaling to zero the sums of position vectors in each kinematic loop of the linkage (e.g. the vector from O to G plus the vector from G to H and the vector from

H to F and finally, the vector from F to O). The matrices one obtains using this approach are detailed in Appendix A for all fingers. For finger W, the velocity equation becomes:

$$\mathbf{A}_W \begin{bmatrix} \dot{\theta_1^B} \\ \dot{\theta_2^B} \\ \dot{\theta_3^B} \end{bmatrix} = \mathbf{V}_W \begin{bmatrix} \dot{\theta_1^F} \\ \dot{\theta_2^F} \\ \dot{\theta_3^F} \\ \dot{\theta_4^F} \end{bmatrix} \tag{3}$$

and matrices $\mathbf{A}_W$ and $\mathbf{V}_W$ are of dimensions 3×3 and 3×4. Please note that since finger W has no crossbeam, the internal angles associated with the connection points of this crossbeam vanish from the left-hand side of the equation. Then, assuming matrix $\mathbf{A}_X$ is not singular (e.g. by numerically computing the condition number of the matrix [29]), one can relate the rate of the driven (non-DOF) angles of the fingers as a function of the DOF with a single matrix:

$$\mathbf{W}_X = {\mathbf{A}_X}^{-1}\mathbf{V}_X \tag{4}$$

with $X \in \{1L, 2L, 1R, 2R, W\}$.

C. Position Analysis

In order to compute the $\mathbf{W}$ matrices defined in Eq. (4), the values of many position vectors must be established. That means one must express the positions of all the joints as functions of DOF. To this aim, expressing the geometric loop-closure of all fingers yields:

$$\begin{aligned} l_1 \begin{bmatrix} {c_1}^F \\ {s_1}^F \end{bmatrix} + l_2 \begin{bmatrix} {c_{12}}^F \\ {s_{12}}^F \end{bmatrix} + l_3 \begin{bmatrix} {c_{123}}^F \\ {s_{123}}^F \end{bmatrix} \\ = l_0 \begin{bmatrix} 1 \\ 1 \end{bmatrix} + l_1 \begin{bmatrix} {c_1}^B \\ {s_1}^B \end{bmatrix} + l_2 \begin{bmatrix} {c_{12}}^B \\ {s_{12}}^B \end{bmatrix} + l_3 \begin{bmatrix} {c_{123}}^B \\ {s_{123}}^B \end{bmatrix} \end{aligned} \tag{5}$$

where

$${c_{i\ldots j}}^U = \cos\left(\sum_{n=i}^{j}\theta_i^U\right), \quad {s_{i\ldots j}}^U = \sin\left(\sum_{n=i}^{j}\theta_i^U\right) \tag{6}$$

and

$$\theta_{i\ldots j}^U = \sum_{n=i}^{j}\theta_i^U \tag{7}$$

with $U \in \{B, F\}$ allowing to distinguish between angles on the front-side (F) or back-side (B) of the finger. Using the shorthand variables a_1, a_2, and a_3 defined in Appendix A, one has:

$$\theta_2^B = 2\arctan\left(\frac{-a_3 - \sqrt{a_3^2 - a_1^2 + a_2^2}}{a_1 - a_2}\right) - \theta_1^B, \tag{8}$$

$$\theta_3^B = \operatorname{atan2}(a_3 + 2l_2^2 {s_{12}}^B, a_2 + 2l_2^2 {c_{12}}^B) - \theta_1^B - \theta_2^B, \tag{9}$$

$$\theta_1^B = \theta_{1234}^F - \theta_{23}^B + \pi. \tag{10}$$

Using the previous equations, all the angles of the 7-bar linkage OABCDEF are defined as functions of θ_1^F, θ_2^F, θ_3^F, θ_4^F. These equations are valid for all fingers but for those with three DOF (1R, 1L, 2R, 2L) one of the previous four angles can be related to the three others. For example, with version 1R the angle θ_1^B can be expressed from θ_1^F, θ_2^F using geometrical equations pertaining to the 5-bar OAIHF, namely:

$$\theta_1^B = 2\operatorname{atan2}\left(\frac{-a_6 - \sqrt{a_6^2 - a_4^2 + a_5^2}}{a_4 - a_5}\right) - \phi_1. \tag{11}$$

where a_4, a_5, and a_6 are also shorthand notations defined in Appendix A. Angle ϕ_i is defined in Fig. 3 and calculated as:

$$\phi_i = \arccos\frac{l_i/2 + \epsilon_i\cos\psi_i}{\sqrt{l_i^2/4 + \epsilon_i^2 + l_i\epsilon_i\cos\psi_i}}, \ i \in [1, 2]. \tag{12}$$

Finally, the angles γ_{1R} and λ_{1R} can be obtained as:

$$\begin{aligned} \gamma_{1R} = \operatorname{atan2}\big[a_6 + 2l_{FH}^2\sin(\theta_1^B + \phi_1), \\ a_5 + 2l_{FH}^2\cos(\theta_1^B + \phi_1)\big] - \theta_{12}^F + \phi_2, \end{aligned} \tag{13}$$

$$\lambda_{1R} = \theta_{12}^F + \gamma_{1R} - \phi_2 - \phi_1 - \theta_1^B. \tag{14}$$

With all the angles of the linkage known, all position vectors can be easily defined and thus, the velocity equations computed.

III. Compliance Model

In order to apply the virtual work principle, the mechanically working forces in the linkage must be established, namely the input actuator force, the output contact forces, and the elastic torque modeling the soft structure of the finger. Indeed, all joints of the fingers are compliant and a pseudo-rigid body model (PBRM) can be used to compute their associated virtual work. This PRBM consists in associating to each joint of the linkages shown in Fig. 2 a virtual rotational spring. The rotational stiffness of these virtual springs is assumed identical for all joints and designated by k while the torque resulting of a rotation of magnitude $\theta - \theta_0$ at a joint is noted t_θ, where θ and θ_0 are the current and at rest angle of the joint respectively. These elastic torques are then simply calculated with:

$$t_\theta = -k(\theta - \theta_0). \tag{15}$$

For all 3-DOF fingers (1L, 2L, 1R, 2R), the total virtual work of the PRBM is:

$$\delta W = \left(\begin{bmatrix} f_a \\ f_1 \\ f_2 \\ f_3 \end{bmatrix}^T {}^4\mathbf{J} + \mathbf{T}_X \begin{bmatrix} \mathbf{0}_{9\times1} & \mathbf{I}_3 \\ & \mathbf{W}_X \end{bmatrix}\right) \begin{bmatrix} \delta x_a \\ \delta\theta_1^F \\ \delta\theta_2^F \\ \delta\theta_3^F \end{bmatrix} \tag{16}$$

with

$$\mathbf{T}_X = \begin{bmatrix} t_{\theta_1^F} & t_{\theta_2^F} & t_{\theta_3^F} & t_{\theta_1^B} & t_{\theta_2^B} & t_{\theta_3^B} & t_{\theta_4^F} & t_{\gamma_X} & t_{\lambda_X} \end{bmatrix} \tag{17}$$

and $X \in \{1L, 2L, 1R, 2R\}$. Again, due to its greater number of DOF and fewer flexures, version W yields a slightly different expression:

$$\delta W = \left(\begin{bmatrix} f_a \\ f_1 \\ f_2 \\ f_3 \\ f_4 \end{bmatrix}^T {}^5\mathbf{J} + \mathbf{T}_W \begin{bmatrix} \mathbf{0}_{7\times1} & \mathbf{I}_4 \\ & \mathbf{W}_W \end{bmatrix}\right) \begin{bmatrix} \delta x_a \\ \delta\theta_1^F \\ \delta\theta_2^F \\ \delta\theta_3^F \\ \delta\theta_4^F \end{bmatrix} \tag{18}$$

with $\mathbf{I}_n$ the $n \times n$ identity matrix and

$$\mathbf{T}_W = \begin{bmatrix} t_{\theta_1^F} & t_{\theta_2^F} & t_{\theta_3^F} & t_{\theta_4^F} & t_{\theta_1^B} & t_{\theta_2^B} & t_{\theta_3^B} \end{bmatrix} \tag{19}$$

For all fingers, ${}^n\mathbf{J}$ is a grasp Jacobian matrix, as defined in [30], of dimension n and ${}^nJ_{ij}$ is the element at the i^{th} line and j^{th} column of that matrix, i.e.:

$$J_{11} = 1, \quad J_{i,1} = -\sin\left(\beta_0 + \sum_{n=1}^{i-1} \theta_i^F\right), \; i \in [2, n] \tag{20}$$

and

$$\begin{cases} J_{i,j} = 0 & i < j, \\ J_{i,j} = d_{i-1} & i = j, \\ J_{i,j} = \sum_{n=j-1}^{i-2} \left(l_n {c_{n+1\ldots i-1}}^F\right) + d_{i-1} & i > j. \end{cases} \tag{21}$$

As a reminder, parameters d_i, l_i and β_0 are defined in Fig. 3 and c_i^F is defined in Eq. (6).

All forces and torques applied to the finger are conservative and therefore, the virtual work of each PRBM is zero at equilibrium, i.e. $\delta W = 0$. Based on this application of the virtual work principle, a relationship between the configuration of the finger defined by the DOF and the produced contact forces can be established. For example, with the three-DOF finger 1R, one has:

$$\begin{bmatrix} f_a \\ f_1 \\ f_2 \\ f_3 \end{bmatrix} = -{}^4\mathbf{J}^{-T}\mathbf{T}_{1R} \begin{bmatrix} \mathbf{0}_{9\times1} & \mathbf{I}_3 \\ & \mathbf{W}_{1R} \end{bmatrix} \tag{22}$$

and therefore, a mathematical relationship can be found between the forces and torques of the fingers. In turn, these forces can be used to establish the stiffness of the fingers as the variation of these forces for a known displacement.

IV. Multi-body/FEA simulations and analysis

To validate the results of Sections II-III, a multi-body simulation software (MSc Adams) was first used and each PRBM of the fingers was built in that software. Torsional springs of identical stiffness were added to all joints in the simulation. Several sets of measurements were obtained for all models in which the angles θ_1^F and θ_2^F are fixed and the forces corresponding to f_1, f_2 and needed to maintain static equilibrium [31] were calculated by the software. This scenario corresponds to a typical power grasp where the object makes contact with the proximal and intermediate phalanges but not on the distal one (hence $f_3 = 0$ and $f_3 = f_4 = 0$ for finger W). A comparison could then be made between the forces obtained from these simulations to the ones produced by using the methodology presented in Section III. The results of one example amongst many of these comparisons between methods is shown in Tab. I for the 1R and W fingers and these results are typical from all simulations. The fingers and grasp scenarios from the latter table include simulations using a Finite Element Analysis (FEA) software, namely Ansys, see Fig. 4. The computed forces from the FEA analyses were recorded and compared to the theoretical forces. As one can plainly see in Tab. I, the differences between both the multibody and FEA softwares with the model from Section III remain small in all cases thereby validating the proposed approach which is more general in terms of design parameters and less computationally intensive.

TABLE I
Force comparison between multibody software (MS), FEA, and theoretical results (TR) in N and for $\theta_1^F = 72.3°$ and $\theta_2^F = 10.0°$

		TR	MS	FEA
Version 1R	f_a	9.6760	9.6750	9.5425
	R_{12}^x	9.6494	9.6738	9.6027
	R_{12}^y	0.8877	0.8878	0.8148
	f_3	0.0210	0	0
Version W	f_a	1.2172	1.2171	1.1986
	R_{12}^x	1.2172	1.2171	1.1987
	R_{12}^y	0.1164	0.1163	0.1187
	f_3	0.0040	0	0
	f_4	0.0024	0	0

R_{12}^x is the resultant of forces f_1 and f_2 on the x-axis, R_{12}^y stands for the same resultant along the y-axis.

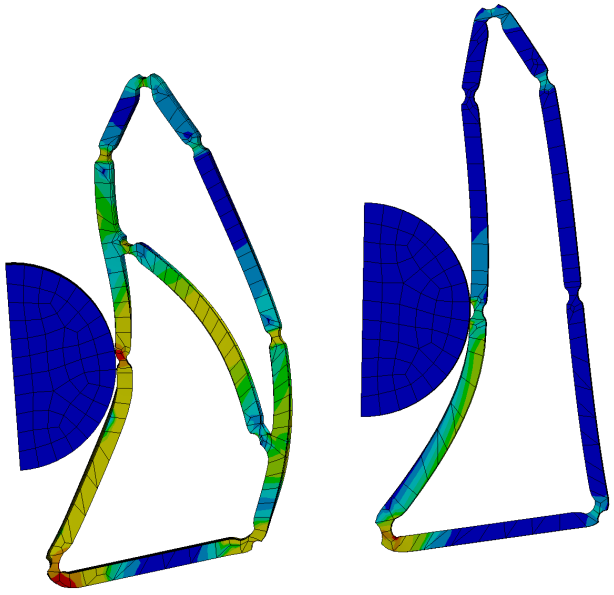

(a) With crossbeam (b) Without crossbeam

Fig. 4. FEA simulations of the fingers from Table I

At this point, the choice of retaining only versions 1R and W of the finger as the most promising designs for prototyping was made based on the results obtained in terms of contact force magnitudes. Both fingers 1R and W exhibited the largest spread for contact forces and are therefore ideal candidates for a finger switching between different stiffness levels. To illustrate this point, the horizontal grasp forces of all fingers are shown in Fig. 5 for the geometrical parameters listed in Tab. II. As can be seen in the figure, the force created by the finger 1R is noticeably greater than all the others and this force is predictably at its lowest with finger W. These plots were created using the same grasp scenario as before, namely that there were no contacts on the distal phalanges and therefore, forces f_3 and f_4 are both equal to zero. Fig 5 also clearly shows that if one switch from the

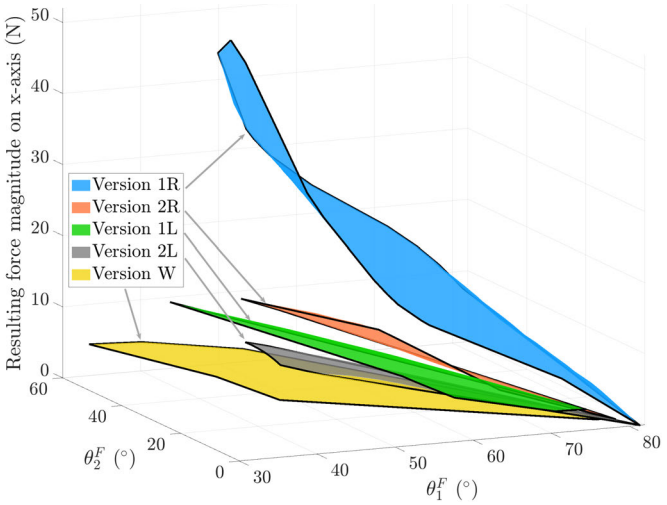

Fig. 5. Norms of the resulting grasp force on x-axis for all versions vs angles θ_1^F, θ_2^F with $f_3 = f_4 = 0$

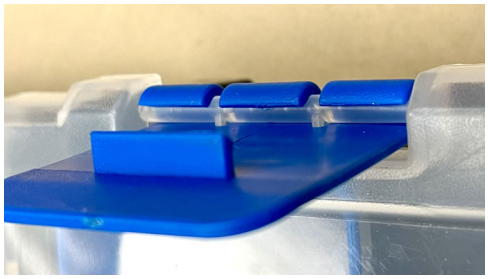

Fig. 6. Snap-fit joint on a mass produced plastic box

three-DOF 1R finger to the four-DOF W finger, a significant drop in the applied forces could be achieved. This switch can be conveniently achieved by disconnecting one of the two attachment point of the crossbeam. To this aim, a snap-fit annular joint design is proposed in this paper [32], [33]. Annular snap-fit joints are a convenient design solution for a revolute joint that can be easily assembled and disassembled during manufacturing and/or operations if needed. See Fig. 6 for an example demonstrating the snap-fit joint used with the lid of a plastic box. Snap-fit are a staple of mass produced consumer goods due to their low cost but they are very rarely been used in robotics research and are proposed here for the first time for kinematic reconfiguration to the best of the authors' knowledge.

TABLE II
GEOMETRICAL PARAMETERS OF THE FINGERS

Angles (°)	ψ_1, ψ_2	β_0	$\theta^F_{1\,0}$	$\theta^F_{2\,0}$	$\theta^F_{3\,0}$	$\theta^F_{4\,0}$
	76.0	8.0	81.3	0.0	150.0	60.0

Lengths (mm)	l_1, l_2	l_3	ϵ_1, ϵ_2	r
	40.0	16.0	3.0	20.0

Stiffness (Nm/rad)	k
	49.54

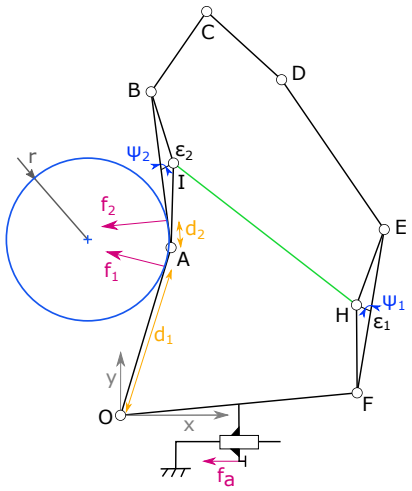

Fig. 7. Illustrative grasp of a cylindrical object

V. OPTIMIZATION

A. Grasp scenario

With the intention of achieving the largest difference in stiffness between the 1R and W fingers, an optimization is now conducted. Since the only change in the design of both fingers is the presence and location of the crossbeam, maximizing this difference in stiffness means one must search for a suitable crossbeam geometry producing the largest stiffness in finger 1R. To define the corresponding optimization problem, a realistic grasp scenario for the finger is first defined, namely the power grasp of a cylindrical object with a diameter r equal to half the length of the proximal phalanx ($l_1/2$) and where the center of this object is located at the same vertical distance as point A (at the intersection of the first two phalanges), see Fig. 7. This cylindrical object is fixed and the finger moves in translation along the x-axis of the reference frame to perform the grasp. The size and position of this target object approximates the intended use case of the gripper, as will be demonstrated in Section VI.

With the grasp geometry accordingly defined, the contact locations at the proximal and intermediate phalanges, d_1 and d_2, characterizing the position of the contact forces f_1 and f_2 between the cylinder and the front phalanges can be readily calculated:

$$\begin{aligned} d_1 &= l_1 - r\ \tan(\theta_2^F/2), \\ d_2 &= r\ \tan(\theta_2^F/2) \end{aligned} \tag{23}$$

where r is the radius of the cylindrical object as defined in Fig. 7. The coordinates $(x_c,\ y_c)$ of the center of this object can also be calculated as:

$$\begin{aligned} x_c &= l_1 \cos(\theta_1^F + \beta_0) - \frac{r\cos(\theta_1^F + \beta_0 + \theta_2^F/2)}{\cos(\theta_2^F/2)}, \\ y_c &= l_1 \sin(\theta_1^F + \beta_0) + \frac{r\cos(\theta_1^F + \beta_0 + \theta_2^F/2)}{\cos(\theta_2^F/2)} \end{aligned} \tag{24}$$

with β_0 and l_1 defined in Fig. 3.

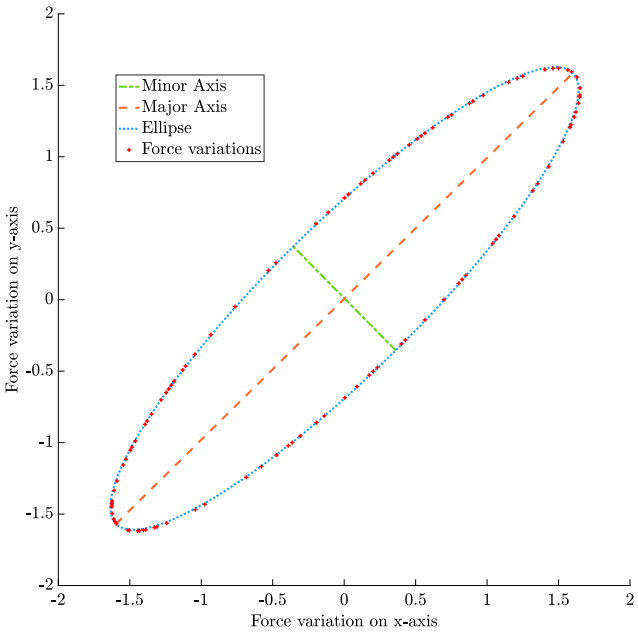

Fig. 8. Force-displacement stiffness ellipsoid for a simulated displacement of 1mm in the plotted directions

B. Optimization Criteria

To conduct the optimization, an evaluation of the grasp stiffness must first be obtained. However, this stiffness is different depending on which direction in the plane is considered (the object being assumed cylindrical, there is no rotational stiffness), and a stiffness matrix characterizes the relationship between forces and displacements. To compute this matrix, a numerical approach was used where small discrete displacements are applied to the object and variations of the grasp forces obtained from Eqs. (22) are recorded. These grasp forces are then projected along the directions of the reference frame, namely the $\mathbf{x}$ and $\mathbf{y}$ axes, and summed up. An example of the resulting force variations from an equilibrium position for a set of displacements is shown in Fig. 8. Values of the parameters used for this figure are the ones from Tab. II and the configuration of the static equilibrium (at rest) for the grasp corresponds to θ_1^F=70.4° and θ_2^F=26.1°.

As one can clearly see from the figure, resulting force variations from a grasp produce an elliptic pattern which is typical for a planar stiffness matrix [34]. The expression of the stiffness matrix corresponding to the geometrical characteristics of the ellipse (major-axis, minor-axis, and the angle ϕ between the major axis and the $\mathbf{x}$-axis) can be found using the approach proposed in [35]. Based on the numerical parameters of the ellipse, eigenvalues (λ_1 and λ_2) and eigenvectors ($\mathbf{e}_1$ and $\mathbf{e}_2$) of the stiffness matrix can be computed. The eigenvectors corresponding to the major and minor axes are respectively:

$$\mathbf{e}_1 = \begin{bmatrix}\cos(\phi)\\ \sin(\phi)\end{bmatrix}, \ \mathbf{e}_2 = \begin{bmatrix}-\sin(\phi)\\ \cos(\phi)\end{bmatrix} \tag{25}$$

and the stiffness matrix then becomes:

$$\mathbf{K} = \begin{bmatrix}k_x & k_{xy}\\ k_{xy} & k_y\end{bmatrix} = \begin{bmatrix}\mathbf{e}_1 & \mathbf{e}_2\end{bmatrix}\begin{bmatrix}\lambda_1 & 0\\ 0 & \lambda_2\end{bmatrix}\begin{bmatrix}\mathbf{e}_1^T\\ \mathbf{e}_2^T\end{bmatrix} \tag{26}$$

TABLE III
OPTIMAL DESIGN PARAMETERS

Parameters	ϵ_1	ϵ_2	ψ_1	ψ_2
Values	4.6 mm	4.7 mm	149.4°	56.1°

TABLE IV
SENSITIVITY OF THE PERFORMANCE INDEX TO VARIATIONS OF THE DESIGN PARAMETERS

Parameters	ϵ_1 $\pm 1\%$	ϵ_2 $\pm 1\%$	ψ_1 $\pm 1\%$	ψ_2 $\pm 1\%$
Perf. Variation	1.72 %	0.78 %	2.50 %	0.87 %

with

$$k_x = \frac{\Delta f_x}{\Delta x_c} \text{ and } k_y = \frac{\Delta f_y}{\Delta y_c}. \tag{27}$$

For example, with the data used in Fig. 8, one obtains:

$$\mathbf{K} = \begin{bmatrix}1.7109 & 0.7919\\ 0.7919 & 1.3564\end{bmatrix}. \tag{28}$$

Different geometries of fingers 1R can now be compared based on their resulting stiffness matrices. Indeed, as previously mentioned, the purpose of the optimization is to maximize the stiffness of finger 1R, which is equivalent to maximizing the smaller of the two eigenvalues of the stiffness matrix [36], [37]. An appropriate optimization index (to be minimized) can therefore be defined as:

$$index = \frac{1}{\min(\lambda_1, \lambda_2)} \tag{29}$$

which will maximize the minimal stiffness of a grasp produced by finger 1R. Note that for the optimization, the stiffness matrix of finger 1R will be calculated with the grasp of a cylindrical object such as the one defined before and shown in Fig. 7.

C. Optimization Parameters and Results

The parameters of the optimization are the ones defining the position of the crossbeam of the finger. Thus, the variables one needs to find are the attachment locations of this crossbeam to the intermediate phalanx and the back proximal link for finger 1R. Using the geometrical parameters defined in Fig. 3, the corresponding variables and their selected ranges are:

- ϵ_1 and ϵ_2 in $[0, 5]$ mm,
- ψ_1 and ψ_2 in $[30, 150]$°.

All the other geometrical parameters stay the same between fingers 1R and W and based on early practical fabrication of finger W, the values listed in Tab. II were selected. The optimization problem therefore has four variables and to solve it, the genetic algorithm tool from *Matlab* was used to minimize the performance index defined in Eq. (29). To ensure the robust convergence of the algorithm to a solution, the tool was run several times with an initial population of 50 individuals and using a maximal of 2,800 generation resulting in the simulation of hundreds of thousands of grasps. This large number of simulations requires fast force computations, i.e. analytical expressions as established in Section III, to be practical. The obtained results are listed in Tab. III. Once these

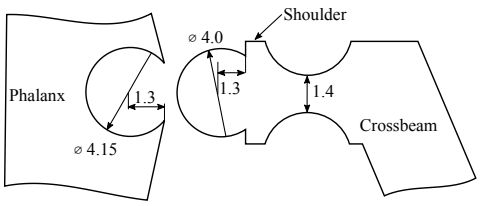

Fig. 9. Selected geometry of annular snap-fit joint

parameters are obtained, the sensitivity of the performance index to each of the optimal parameters was also studied. Tab. IV shows the absolute values of the average change in value of the optimization index for a $\pm 1\%$ deviation of the optimal parameters. The most influential design parameter is ψ_1 as this 1% variation of its value yields a 2.50% variation of the global performance criterion. Conversely, ϵ_2 is the parameter with the weakest impact on the optimization criteria (0.87%).

VI. Experiments

Finally, a prototype of the soft finger with the optimal parameters previously obtained was 3D printed in thermoplastic polyurethane (TPU, shore 95A, red) in order to proceed with experimental validation of the change in stiffness and its usefulness in practical applications. To toggle between the two stiffness modes a geometry of snap-fit joint was designed similar to the one illustrated in Fig. 6. The geometry of this snap-fit is shown in Fig. 9. This particular geometry was designed through experimentation with various values of clearances to ensure a proper fit and includes a shoulder to prevent the rotation of its circular part inside the associated cavity during the grasp in order for the flexure of the crossbeam to deform and produce the same elastic torque as the other joints. Practical considerations on the geometry of the snap-fit joints limits the maximal forces that the finger can applied before buckling occurs. A 3D CAD view of the optimal finger using this snap-fit is presented in Fig. 10. This finger was 3D printed twice and the two fingers are shown in Fig. 11 grasping a metal canister both in low- and high-stiffness mode. The specific design of the snap-fit shown in Fig. 9 allows for minimal interferences between the disconnected crossbeam and the front and back links of the finger as the crossbeam simply slides on these links.

A. Characterization

To characterize the finger in terms of stiffness, a test bench was designed using a force sensor attached to a motorized translational stage (eTrack series from Newmark) in order to compare the forces produced by the finger as a function of displacements in both the stiff and soft modes, see Fig. 12. The force sensor used is a traction-compression load cell (3138 S-type 100kg) with a Wheatstone bridge including a USB compatible output (PhidgetBridge 4-Input 1046_0). A *Labview* software handles both the movement of the translational stage and load cell measurements synchronously. The artifact object used for characterization is a 40 mm cylinder attached to

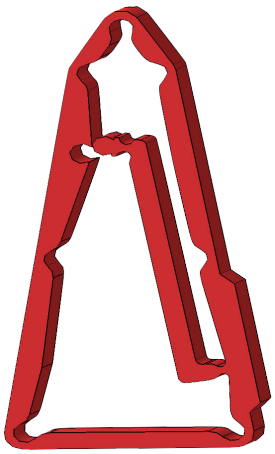

Fig. 10. CAD of the finger

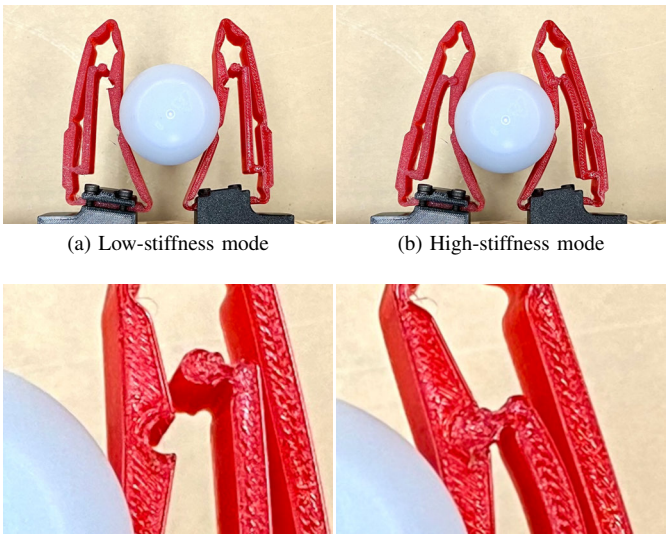

(a) Low-stiffness mode (b) High-stiffness mode

(c) Snap-fit joint disengaged in low-stiffness mode (zoom) (d) Snap-fit joint engaged in high-stiffness mode (zoom)

Fig. 11. Low- and high-stiffness grasp examples of the optimal fingers

the force sensor and linear stage thereby allowing to apply a precise displacement while measuring the resulting force. Forces were measured in discrete steps of 0.4 mm displacements. To compare between the two stiffness mode, three sets of force measurements are obtained for contact points at different locations on the front face of the finger with or without the internal crossbeam engaged. The resulting force profiles are shown in Fig. 13, each color stands for a specific contact location on the finger while solid lines correspond to the high-stiffness mode and dotted lines to the low-stiffness mode. Fig. 14 shows the x-axis stiffness computed from the forces of Fig. 13. Note that the values of the (instantaneous) stiffnesses changes for the different displacements of the finger as one could expect, the finger being a complex mechanism, but these stiffnesses follow a similar trend both in low- and high-stiffness modes so their ratios tend to stay around the same values.

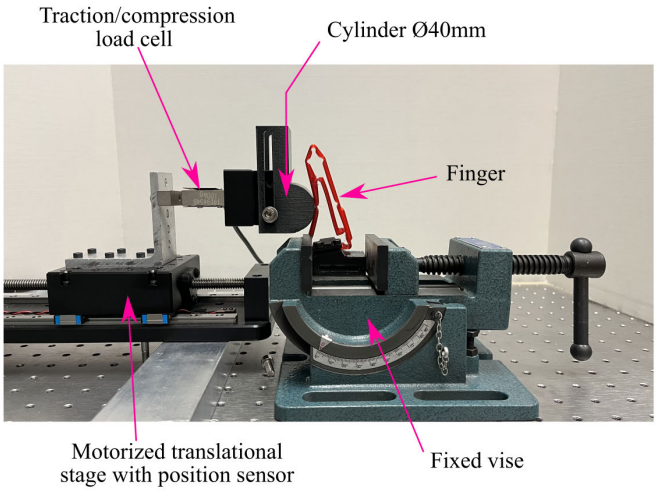

Fig. 12. Characterization test bench.

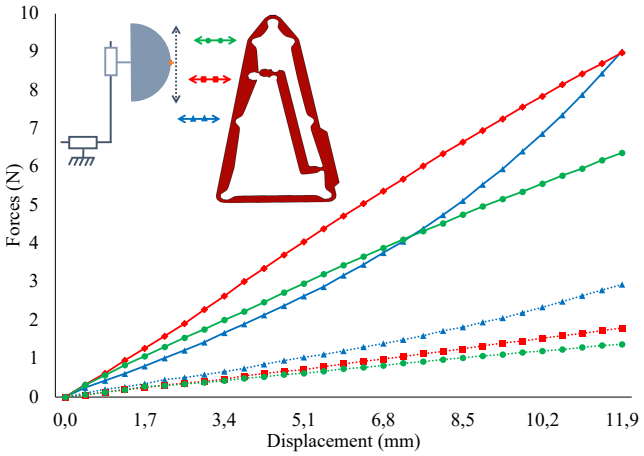

Fig. 13. Resulting horizontal contact forces in the two stiffness modes (solid lines: finger 1R, dotted lines: finger W) for different positions of a cylindrical object (Ø40mm), see arrows in upper left corner.

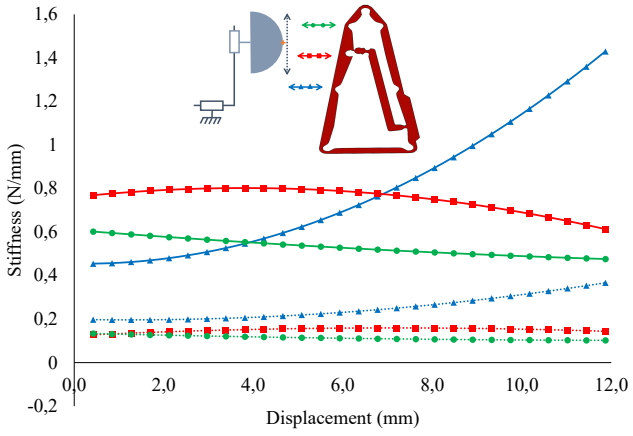

Fig. 14. Computed $\mathbf{x}$-axis stiffness in the two stiffness modes (solid lines: version 1R, dotted lines: version W) for different positions of a cylindrical object (Ø40mm), see arrows.

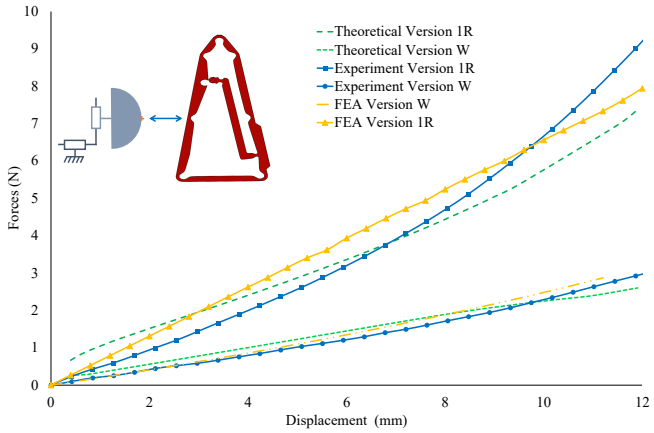

Fig. 15. Comparison between the forces from the theoretical model, the FEA analysis and experimental measurements with the prototype for a cylindrical object contact (Ø40mm) at the blue arrow location.

TABLE V
STIFFNESS RATIOS

Contact position (see Figs. 13-14)	Low	Middle	High
Stiffness ratio	3.76	5.02	4.79
Average stiffness ratio		4.52	

The experimental ratios of the stiffness between the high- and low-stiffness modes are listed in Tab. V. On average, the stiffness is amplified by a factor of more than 4 when the snap-fit joint is engaged and the crossbeam contributes to the grasps. From these results one can also see that the stiffness of the finger tends to be greater when a contact occurs closer to the base of the finger. This also points out that fragile objects should be grasped with the most distal part of the finger that is physically achievable. Fig. 15 shows a comparison between the forces computed with the theoretical model and the forces measured with the prototype. Results are consistent as the plots stay generally close over the whole grasp range. However, there is a notable difference between these forces when large displacements are considered. This discrepancy is conjectured to come from two combined causes. First, when excessively large deformations occur the internal crossbeam makes contact with the back of the finger. This is why with large displacements the measured forces are noticeably greater than predicted by the theoretical model. A second source of error comes from the difficulty of achieving an accurate torque model for the compliant joints. Indeed, a simple linear equation was used while for large displacements, the actual force-deformation relationship might be more complex. Additionally, for large displacements, links that were assumed rigid also slightly bend and contribute to the deformation of the finger. Yet and despite these inaccuracies, the proposed model clearly demonstrated its efficiency to capture the most important parts of the finger force-displacement relationship and shows a similar degree of precision as the FEA simulation that is far more computationally intensive. To validate the previous results, additional FEA simulations were conducted using Ansys with the produced optimal finger, similarly to the ones from Section IV. These simulations allowed to val-

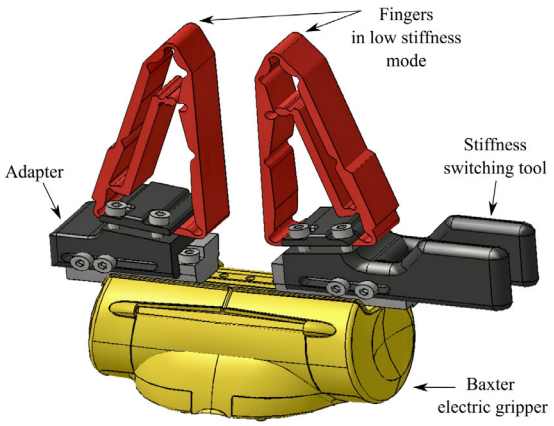

Fig. 16. CAD model of the hand assembly on the Baxter robot

idate both the theoretical model and the optimization results. Comparisons are shown in Fig. 15 and again demonstrate an excellent degree of correspondence between the different models and the experiments.

B. Stiffness Mode Switch

After the characterization of the prototyped fingers, these fingers were used in a more practical scenario, i.e. with the actual gripper of a robot and more specifically a Baxter collaborative robot. This cobot was developed by the company Rethink Robotics and was commercialized from September 2011. It is a humanoid robot without legs but with two seven-DOF arms. These arms are equipped in this work with their standard electric grippers (40 mm translation total stroke) which set the achievable grasp force range as the latter is not a property of the fingers but of the gripper onto which they are affixed. To attach the fingers on these electric grippers, plastic adapters were designed and 3D printed. These adapters have two roles, the first and most obvious is to provide a way of attaching the flexible fingers to the translating parts of the gripper but a second important role is to allows for the connection and disconnection of the snap-fit joint in order for the robot to be able to change the stiffness mode of the finger on its own. The CAD model of these adapters connecting the fingers to the electric gripper shown in Fig. 16.

The procedure for engagement and disengagement of the crossbeam using the stiffness switching tool of the adapter is illustrated by Figs. 17 and 18. The engagement is shown in Fig. 17 and is the easiest of the two procedures. The tip of the finger attached to one hand of the robot is inserted into the stiffness switching tool of the other hand. This tool is simply constituted by two rigid beams separated by a small distance sufficient to insert the soft finger and its geometry can be adjusted to various sizes of snap-fit joints and crossbeams. As shown in Fig. 17b, the compression of each side of the finger during insertion engages the crossbeam. The second procedure, i.e. the disconnection of the snap-fit joint, is shown in Fig. 18. One prong of the stiffness switching tool is inserted between the front links of the finger and the crossbeam (Fig. 18a). Then, a rotating motion of the tool pulls on the snap-fit joint and disengages it from the phalanx it was attached to (Fig. 18b). Of course, this two-pronged stiffness switching tool can also be attached to a support structure inside the robot workspace, i.e. it does not need to be part of the adapters to the gripper but it is convenient to use when located there.

The engagement force of the snap fit was measured with a load cell (Shimpo FGV-100XY) and average to 0.73 kg (with a 0.08 standard deviation) which correlates well with the predicted mating force $W = 0.76$ kg for annular snap fit, considering the part are 3D printed. The predicted mating force of this geometry of joint can be found in [32] as:

$$W = P\frac{\mu + \tan\alpha}{1 - \mu\tan\alpha} \tag{30}$$

$$\text{with } P = ydEX_n \tag{31}$$

$$\text{and } X_n = 0.62\frac{\sqrt{(d_0/d-1)/(d_0/d+1)}}{((d_0/d)^2+1)/((d_0/d)^2-1)+\nu)} \tag{32}$$

using $\mu = 0.36$ as the friction coefficient, $\alpha = 69.3°$ as the joint lead angle, $y = 0.15$ mm as the undercut, $d = 4$ mm and $d_0 = 4.5$ mm as the inside and external diameter of the joint, $E = 30.7$ MPa as secant modulus, and where $\nu = 0.3$ is Poisson's ratio. All parameters are constant for a geometry of snap fit joint.

Because the switch from high to low stiffness modes requires the insertion of a fixture prong between the back of the finger and the crossbeam, sufficient space needs to be available. This insertion could be addressed explicitly in the optimization of the design by introducing a geometric constraint in the procedure be discussed in Section V to handle the case when one would converge to a solution where this space is insufficient. For instance a penalty function could be added to Eq. 29 to ensure a minimal circle can be inserted in the finger, see [38] for a similar approach.

C. Grasp Experiments and Payload Comparison

To illustrate the ability of the fingers to grasp different objects and the usefulness of their dual stiffness capability, the grasps of various household and common objects were carried out, first in high stiffness mode see Fig. 19. Indeed, for heavier objects, the low stiffness mode fails and is not capable of producing forces large enough to secure the objects (see Figs. 20a,b,c). In these cases, the higher stiffness mode need to be engaged in order to successfully pick up the objects, see Fig. 20d,e. However, the high stiffness mode cannot be used for all objects as it can lead to damages with fragile objects. This is especially important and a constraint with delicate agricultural produces and food items. For instance, in Fig 21, a broccoli flower, a biscuit, a croissant, and a maki are all severely damaged when grasped in high stiffness mode while they suffer only minor deformations with the low stiffness mode. In Fig. 21 both the broccoli and croissant for example exhibit a significant and permanent deformation after the grasp

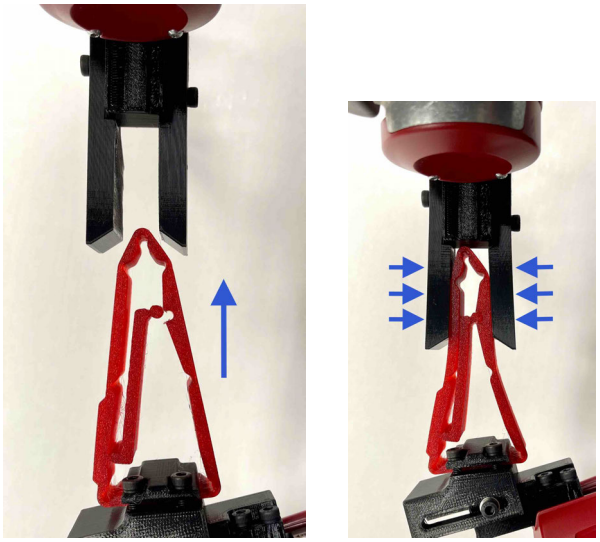

(a) (b)

Fig. 17. Engagement of the snap-fit joint: (a) insertion of the finger, (b) pinching motion of the fingertip. The same pinch can be obtained by the fingers themselves as a tool, see multimedia attachment.

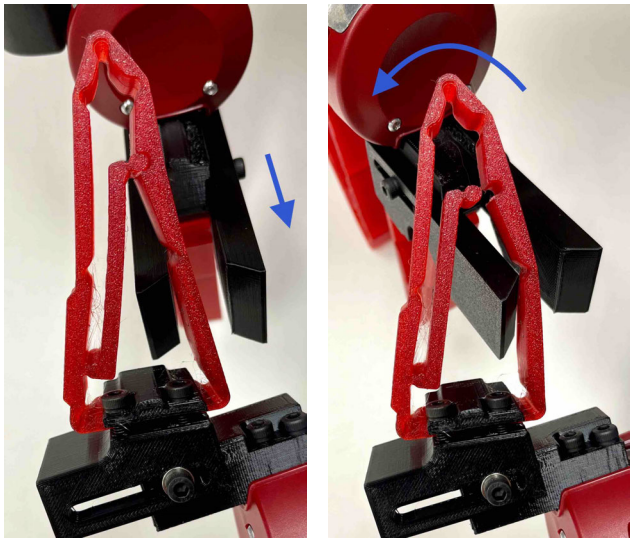

(a) (b)

Fig. 18. Disengagement of the snap-fit joint: (a) introduction of the switching tool between the phalanges and the crossbeam; (b) Twisting of the tool to disconnect the joint. Again, the same effect can be obtained by the fingers themselves as a tool, see multimedia attachment.

in high-stiffness mode resulting in an unappealing product for the customer. Note that in both cases the fingers are position controlled and the space between them at the bottom remains the same in both modes. Therefore, in the absence of tactile or force sensing, switching to low stiffness mode for fragile objects is a simple yet efficient solution. All quantitative data corresponding to the objects used in this Section are listed in Tab. VI.

Additionally, a series of experiments were conducted to estimate the payload of the electric gripper when equipped with the proposed finger and compare it to other tools. To this effect,

TABLE VI
QUANTITATIVE DATA ON GRASPED OBJECTS

	Size (mm)	Weight	Shape
Water bottle (Fig.19a)	60x60x190	500g	Cylindrical
Toothpaste (Fig.19b)	45x45x150	160g	Cylindrical
Screwdriver (Fig.19c)	30x30x260	165g	Complex
Pliers (Fig.19d)	50x15x210	350g	Complex
Soap bars (Fig.20)	50x80x120	300g	Parallelepipedic
Broccoli flower (Fig.21a)	40x40x40	30g	Complex
Biscuit (Fig.21b)	60x60x20	20g	Cylindrical
Croissant (Fig.21c)	125x65x40	50g	Complex
Maki (Fig.21d)	50x50x20	30g	Cylindrical

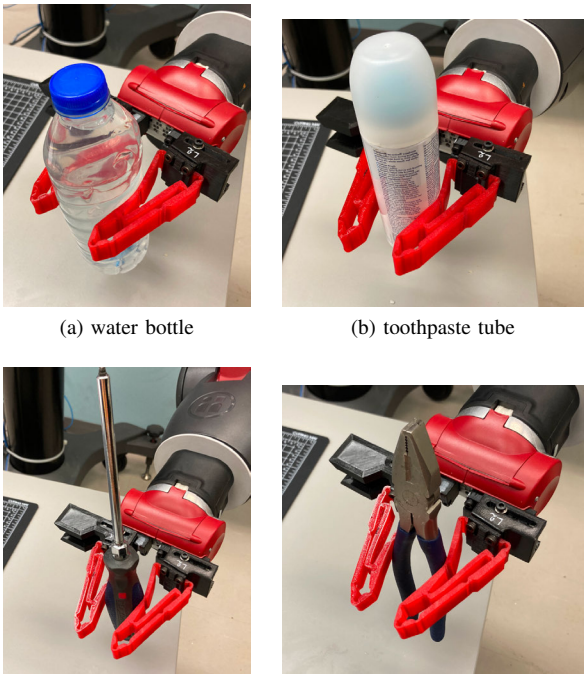

(a) water bottle (b) toothpaste tube

(c) screwdriver (d) plier

Fig. 19. Grasps of various household objects in high-stiffness mode.

the pullout force of a standardized Schedule 40 PVC pipe out of the gripper as proposed in [39], [40] was measured and compared to the same gripper when equipped with: Festo DHAS fingers, a rigid finger with soft round contact pad (printed with 5% infill ratio), the same rigid finger with stiff contact pads, see Fig. 22. All contact surfaces are made from the same TPU material used to manufacture both our and Festo's fingers to quantify the intrinsic performance of the kinematic structure proposed in this paper, independently from contact material effects. Similarly, the same electric gripper was commanded with the same input (maximal closing force and stroke) to remove dependence to the gripper characteristics. The results are listed in Tab. VII and indicate that the newly proposed finger has a significantly better payload than Festo's original design while providing a greater adaptability than rigid finger with pads in addition to a unique selectable stiffness. The grasp range of all grippers are 0-80 mm and the usable finger length is 95 mm.

(a) (b) (c)

(d) (e)

Fig. 20. A failed grasp of soap bars in low-stiffness mode (a,b,c) becomes successful (d,e) in high-stiffness mode

TABLE VII
PAYLOAD ESTIMATION THROUGH PULLOUT TEST

	Average (kg)	STD (kg)
Proposed finger (soft mode)	0.27	0.05
Proposed finger (hard mode)	0.56	0.04
Festo DHAS finger	0.30	0.03
Rigid finger w/ soft pad	0.77	0.11
Rigid finger w/ stiff pad	0.75	0.02

VII. CONCLUSION

This article presented the design of a novel soft finger, inspired by the Fin Ray Effect, that can switch from a low- to high-stiffness. First, the kinematic analysis of these fingers with one or no crossbeam was conducted in order to be able to predict the forces they generate and thus, their resulting grasp stiffness. Then, an optimization aiming at producing fingers with the largest difference between the soft and stiff modes was shown. In future work, this optimization could include all potential designs shown in Fig. 2. A novel technique allowing to switch from one design to the other and based on the introduction of an annular snap-fit joint was then presented. This snap-fit reconfiguration allows for the changing of the kinematic structure of the finger which yields a very different behavior of the finger. A greater range of stiffness variation could also be achieved using multiple internal crossbeams equipped with similar detachable snap-fit joints. Finally, a prototype was 3D printed and experiments were conducted to measure the actual stiffness of the two modes and show how one can switch between modes without adding new actuators, as well as to illustrate that stiffness levels can be adapted to practical grasp scenarios. Engaging or disengaging crossbeams in a soft finger is a simple and efficient technique to provide robots or cobots with a finer degree of force control that can be typically achieved using commonly driven pneumatic or electric grippers due to practical issues such as backlash and friction, e.g. [41]. With the proposed finger, the same displacement of the gripper actuator can result in a greatly different grasp stiffness for the seized objects and thus, largely varying grasp forces. The stiffness switch we conducted took approximately 4s with our Baxter robot which

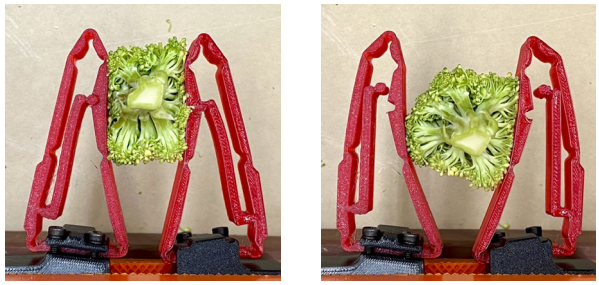

(a) Broccoli

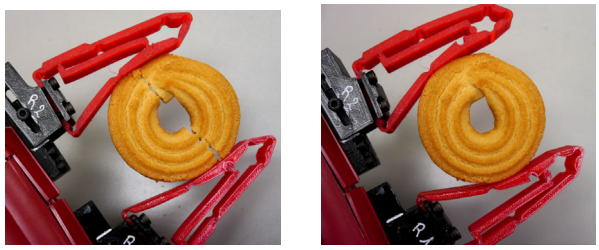

(b) Biscuit

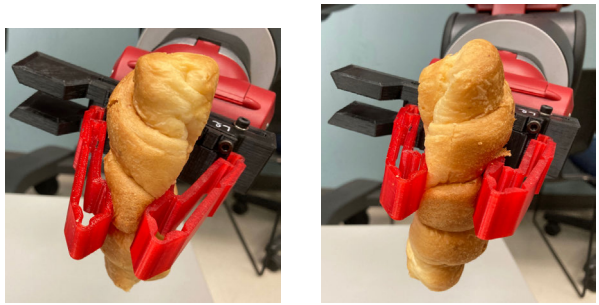

(c) Croissant

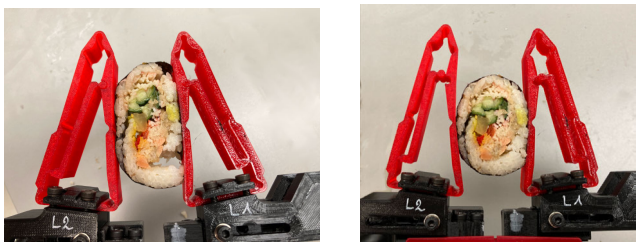

(d) Maki

Fig. 21. Bruising/breaking/crushing of various delicate food items and produces in high-stiffness mode (left) and their corresponding gentle envelopment in low-stiffness mode (right)

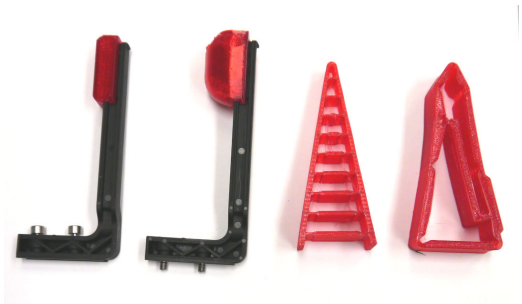

Fig. 22. Compared fingers: rigid link with thin TPU pad, rigid link with large soft TPU pad, Festo DHAS finger, the proposed new finger (from left to right, adapters removed from the last two fingers)

is only consistently slower than bulk locking but outperforms most other methods and is orders of magnitude faster than material change techniques (e.g. low melting point alloys, shape memory polymers, biomaterials, etc.) [12]. The required duration for a stiffness switch of our fingers is only limited by the dynamics of the handling robot and faster robots could achieve dramatically faster switches. Furthermore, while stiffness change of bulk locking is indeed generally very fast, the stiffness variation the latter produces is actually small compared to our technique. For instance, a maximal stiffness variation of 36 % is reported in [15] while the average stiffness variation we measured is 452 %. This change of stiffness achieved with out proposed design is greater than what can be obtained with fluidic and braided sleeve structures or electroactive polymers and similar to the range of magnetorheological elastomers [13]. See the latter reference for more details on other stiffness changing techniques in soft robotics.

APPENDIX
GEOMETRIC COEFFICIENTS

$$\begin{aligned} a_1 =& 2l_1^2 + 2l_2^2 + l_0^2 + 2l_1[l_2 {c_2}^F + l_3 {c_{23}}^F \\ & - l_0({c_1}^F + {s_1}^F) - l_1\cos(\theta_1^F - \theta_1^B)] \\ & + 2l_2[l_3 {c_3}^F - l_0({c_{12}}^F + {s_{12}}^F) \\ & - l_1\cos(\theta_{12}^F - \theta_1^B)] + 2l_0 l_1({c_1}^B + {s_1}^B) \\ & - 2l_3(l_0({c_{123}}^F + {s_{123}}^F) + l_1\cos(\theta_{123}^F - \theta_1^B)), \end{aligned} \tag{33}$$

$$a_2 = -2l_2(l_1 {c_1}^F + l_2 {c_{12}}^F + l_3 {c_{123}}^F - l_0 - l_1 {c_1}^B), \tag{34}$$

$$a_3 = -2l_2(l_1 {s_1}^F + l_2 {s_{12}}^F + l_3 {s_{123}}^F - l_0 - l_1 {s_1}^B) \tag{35}$$

$$\begin{aligned} a_4 =& l_1^2 + l_0^2 + l_{FH}^2 + l_{AI}^2 - l_{HI}^2 \\ & + 2l_1(l_{AI}\cos(\theta_2^F - \phi_2) - l_0({c_1}^F + {s_1}^F)) \\ & + 2l_{AI} l_0(\cos(\theta_{12}^F - \phi_2) + \sin(\theta_{12}^F - \phi_2)) \end{aligned} \tag{36}$$

$$a_5 = -2l_{FH}(l_1 {c_1}^F + l_{AI}\cos(\theta_{12}^F - \phi_2) - l_0) \tag{37}$$

$$a_6 = -2l_{FH}(l_1 {s_1}^F + l_{AI}\sin(\theta_{12}^F - \phi_2) - l_0). \tag{38}$$

APPENDIX
KINEMATIC MATRICES

$$\mathbf{A}_{1R} = \begin{bmatrix} \mathbf{Er}_{FC} & \mathbf{Er}_{EC} & \mathbf{Er}_{DC} & & \mathbf{0}_{2\times3} & \\ \mathbf{Er}_{FI} & & \mathbf{0}_{2\times4} & & & \mathbf{Er}_{HI} \\ 1 & 1 & 1 & -1 & 0 & 0 \\ 1 & 0 & 0 & 0 & -1 & 1 \end{bmatrix} \tag{39}$$

$$\mathbf{A}_{2R} = \begin{bmatrix} \mathbf{Er}_{FC} & \mathbf{Er}_{EC} & \mathbf{Er}_{DC} & & \mathbf{0}_{2\times3} & \\ \mathbf{Eu} & \mathbf{Ev} & \mathbf{0}_{2\times3} & & & \mathbf{Er}_{JG} \\ 1 & 1 & 1 & -1 & 0 & 0 \\ 1 & 1 & 0 & 0 & -1 & 1 \end{bmatrix} \tag{40}$$

with

$$\mathbf{u} = \mathbf{r}_{FJ} + \mathbf{r}_{GJ} \text{ and } \mathbf{v} = \mathbf{r}_{EJ} + \mathbf{r}_{GJ} \tag{41}$$

$$\mathbf{A}_{1L} = \begin{bmatrix} \mathbf{Er}_{FC} & \mathbf{Er}_{EC} & \mathbf{Er}_{DC} & & \mathbf{0}_{2\times3} & \\ \mathbf{Er}_{FG} & & \mathbf{0}_{2\times4} & & & \mathbf{Er}_{HG} \\ 1 & 1 & 1 & -1 & 0 & 0 \\ 1 & 0 & 0 & 0 & -1 & 1 \end{bmatrix} \tag{42}$$

$$\mathbf{A}_{2L} = \begin{bmatrix} \mathbf{Er}_{FC} & \mathbf{Er}_{EC} & \mathbf{Er}_{DC} & & \mathbf{0}_{2\times3} & \\ \mathbf{Er}_{FI} & \mathbf{Er}_{EI} & \mathbf{0}_{2\times3} & & & \mathbf{Er}_{JI} \\ 1 & 1 & 1 & -1 & 0 & 0 \\ 1 & 0 & 0 & 0 & -1 & 1 \end{bmatrix} \tag{43}$$

$$\mathbf{A}_W = \begin{bmatrix} \mathbf{Er}_{FC} & \mathbf{Er}_{EC} & \mathbf{Er}_{DC} \\ 1 & 1 & 1 \end{bmatrix} \tag{44}$$

$$\mathbf{V}_{1R} = \mathbf{V}_{2L} = \begin{bmatrix} \mathbf{Er}_{OC} & \mathbf{Er}_{AC} & \mathbf{Er}_{BC} \\ \mathbf{Er}_{OI} & \mathbf{Er}_{AI} & \mathbf{0}_{2\times1} \\ 1 & 1 & 1 \\ 1 & 1 & 0 \end{bmatrix} \tag{45}$$

$$\mathbf{V}_{2R} = \mathbf{V}_{1L} = \begin{bmatrix} \mathbf{Er}_{OC} & \mathbf{Er}_{AC} & \mathbf{Er}_{BC} \\ \mathbf{Er}_{OG} & \mathbf{0}_{2\times2} & \\ 1 & 1 & 1 \\ 1 & 0 & 0 \end{bmatrix} \tag{46}$$

$$\mathbf{V}_W = \begin{bmatrix} \mathbf{Er}_{OC} & \mathbf{Er}_{AC} & \mathbf{Er}_{BC} & \mathbf{0}_{2\times1} \\ 1 & 1 & 1 & 1 \end{bmatrix} \tag{47}$$

$$\mathbf{E} = \begin{bmatrix} 0 & -1 \\ 1 & 0 \end{bmatrix}, \ \mathbf{I}_2 = \begin{bmatrix} 1 & 0 \\ 0 & 1 \end{bmatrix} \tag{48}$$

$\mathbf{0}_{m\times n}$ is the m-row and n-column zero matrix.

ACKNOWLEDGMENTS

The support of the Natural Sciences and Engineering Research Council of Canada (grant RGPIN327005) is gratefully acknowledged.

REFERENCES

[1] N. Mouazé and L. Birglen, "Bistable compliant underactuated gripper for the gentle grasp of soft objects," *Mechanism and Machine Theory*, vol. 170, p. 104676, 2022.

[2] L. Birglen and T. Schlicht, "A statistical review of industrial robotic grippers," *Robotics and Computer-Integrated Manufacturing*, vol. 49, pp. 88–97, 2018.

[3] R. Wood and C. Walsh, "Smaller, softer, safer, smarter robots," pp. 210ed19–210ed19, 2013.

[4] R. Liang, G. Xu, B. He, M. Li, Z. Teng, and S. Zhang, "Developing of a rigid-compliant finger joint exoskeleton using topology optimization method," in *2021 IEEE International Conference on Robotics and Automation (ICRA)*. IEEE, 2021, pp. 10 499–10 504.

[5] Y. Li, M. Congr, D. Liu, and Y. Du, "Design and analysis of a novel lightweight, versatile soft-rigid robot," in *2021 IEEE International Conference on Robotics and Automation (ICRA)*. IEEE, 2021, pp. 11 871–11 877.

[6] R. Bannasch and L. Kniese, "Manipulator tool and holding and/or expanding tool with at least one manipulator tool," Dec. 18 2012, uS Patent 8,333,417.

[7] C. Armanini, I. Hussain, M. Z. Iqbal, D. Gan, D. Prattichizzo, and F. Renda, "Discrete cosserat approach for closed-chain soft robots: Application to the fin-ray finger," *IEEE Transactions on Robotics*, vol. 37, no. 6, pp. 2083–2098, 2021.

[8] C. Tawk, R. Mutlu, and G. Alici, "A 3d printed modular soft gripper integrated with metamaterials for conformal grasping," *Frontiers in Robotics and AI*, vol. 8, 2022.

[9] S. Liu, F. Wang, Z. Liu, W. Zhang, Y. Tian, and D. Zhang, "A two-finger soft-robotic gripper with enveloping and pinching grasping modes," *IEEE/ASME Transactions on Mechatronics*, vol. 26, no. 1, pp. 146–155, 2020.

[10] M. Xie, M. Zhu, Z. Yang, S. Okada, and S. Kawamura, "Flexible self-powered multifunctional sensor for stiffness-tunable soft robotic gripper by multimaterial 3d printing," *Nano Energy*, vol. 79, p. 105438, 2021.

[11] D. D. Arachchige, Y. Chen, I. D. Walker, and I. S. Godage, "A novel variable stiffness soft robotic gripper," in *2021 IEEE 17th International Conference on Automation Science and Engineering (CASE)*. IEEE, 2021, pp. 2222–2227.

[12] L. Blanc, A. Delchambre, and P. Lambert, "Flexible medical devices: Review of controllable stiffness solutions," in *Actuators*, vol. 6, no. 3. Multidisciplinary Digital Publishing Institute, 2017, p. 23.

[13] M. Manti, V. Cacucciolo, and M. Cianchetti, "Stiffening in soft robotics: A review of the state of the art," *IEEE Robotics & Automation Magazine*, vol. 23, no. 3, pp. 93–106, 2016.

[14] S. Wolf, G. Grioli, O. Eiberger, W. Friedl, M. Grebenstein, H. Höppner, E. Burdet, D. G. Caldwell, R. Carloni, M. G. Catalano *et al.*, "Variable stiffness actuators: Review on design and components," *IEEE/ASME transactions on mechatronics*, vol. 21, no. 5, pp. 2418–2430, 2015.

[15] M. Cianchetti, T. Ranzani, G. Gerboni, I. De Falco, C. Laschi, and A. Menciassi, "Stiff-flop surgical manipulator: Mechanical design and experimental characterization of the single module," in *2013 IEEE/RSJ international conference on intelligent robots and systems*. IEEE, 2013, pp. 3576–3581.

[16] D. Petković, M. Issa, N. D. Pavlović, L. Zentner, and Ž. Ćojbašić, "Adaptive neuro fuzzy controller for adaptive compliant robotic gripper," *Expert Systems with Applications*, vol. 39, no. 18, pp. 13 295–13 304, 2012.

[17] E. Brown, N. Rodenberg, J. Amend, A. Mozeika, E. Steltz, M. R. Zakin, H. Lipson, and H. M. Jaeger, "Universal robotic gripper based on the jamming of granular material," *Proceedings of the National Academy of Sciences*, vol. 107, no. 44, pp. 18 809–18 814, 2010.

[18] M. Cianchetti, T. Ranzani, G. Gerboni, T. Nanayakkara, K. Althoefer, P. Dasgupta, and A. Menciassi, "Soft robotics technologies to address shortcomings in today's minimally invasive surgery: The stiff-flop approach," *Soft Robotics*, vol. 1, no. 2, pp. 122–131, 2014. [Online]. Available: https://doi.org/10.1089/soro.2014.0001

[19] M. Cox, D. Wang, J. Barés, and R. P. Behringer, "Self-organized magnetic particles to tune the mechanical behavior of a granular system," *EPL (Europhysics Letters)*, vol. 115, no. 6, p. 64003, 2016.

[20] W. Shan, T. Lu, Z. Wang, and C. Majidi, "Thermal analysis and design of a multi-layered rigidity tunable composite," *International Journal of Heat and Mass Transfer*, vol. 66, pp. 271–278, 2013.

[21] M. Liu, L. Hao, W. Zhang, and Z. Zhao, "A novel design of shape-memory alloy-based soft robotic gripper with variable stiffness," *International journal of advanced robotic systems*, vol. 17, no. 1, p. 1729881420907813, 2020.

[22] X. Li, W. Chen, W. Lin, and K. H. Low, "A variable stiffness robotic gripper based on structure-controlled principle," *IEEE Transactions on Automation Science and Engineering*, vol. 15, no. 3, pp. 1104–1113, 2017.

[23] K. Chandrasekaran, A. Somayaji, and A. Thondiyath, "A novel design for a compliant mechanism based variable stiffness grasper through structure modulation," *Journal of Medical Devices*, vol. 15, no. 1, 2021.

[24] Y. She, H.-J. Su, C. Lai, and D. Meng, "Design and prototype of a tunable stiffness arm for safe human-robot interaction," in *International Design Engineering Technical Conferences and Computers and Information in Engineering Conference*, vol. 50169. American Society of Mechanical Engineers, 2016, p. V05BT07A063.

[25] P. Kuppens, M. Bessa, J. L. Herder, and J. Hopkins, "Compliant mechanisms that use static balancing to achieve dramatically different states of stiffness," *Journal of Mechanisms and Robotics*, vol. 13, no. 2, 2021.

[26] X. Shan and L. Birglen, "Modeling and analysis of soft robotic fingers using the fin ray effect," *The International Journal of Robotics Research*, vol. 39, no. 14, pp. 1686–1705, 2020.

[27] L. Howell, *Compliant Mechanisms*, ser. A Wiley-Interscience publication. Wiley, 2001.

[28] R. L. Norton, *Design of machinery: an introduction to the synthesis and analysis of mechanisms and machines*. McGraw-Hill/Higher Education, 2008.

[29] J.-P. Merlet, "Jacobian, manipulability, condition number, and accuracy of parallel robots," 2006.

[30] L. Birglen, "Enhancing versatility and safety of industrial grippers with adaptive robotic fingers," in *2015 IEEE/RSJ international conference on intelligent robots and systems (IROS)*. IEEE, 2015, pp. 2911–2916.

[31] G. A. Kragten and J. L. Herder, "The ability of underactuated hands to grasp and hold objects," *Mechanism and Machine Theory*, vol. 45, no. 3, pp. 408–425, 2010. [Online]. Available: https://www.sciencedirect.com/science/article/pii/S0094114X09001797

[32] B. M. S. T. Report, *Snap-Fit Joints for Plastics - a design guide*. Bayer Material Science Technical Report, 2010.

[33] B. Raucent, C. Nederlandt, and D. Johnson, "Plastic snapfit fastener design," *The International Journal of Advanced Manufacturing Technology*, vol. 14, no. 3, pp. 185–198, 1998.

[34] J. Selig, "Synthesis of planar stiffness," in *IMA Conference on Mathematics of Robotics*. Springer, 2020, pp. 25–36.

[35] H. P. Gavin, "Mathematical properties of stiffness matrices," *Lecture notes for Matrix Structural Analysis, CEE421L, Department of Civil and Environmental Engineering, Duke University*, vol. 2, pp. 1–6, 2006.

[36] C. Gosselin *et al.*, "Stiffness mapping for parallel manipulators," *IEEE transactions on Robotics and Automation*, vol. 6, no. 3, pp. 377–382, 1990.

[37] H. Dong, C. Qiu, D. K. Prasad, Y. Pan, J. Dai, and I.-M. Chen, "Enabling grasp action: Generalized quality evaluation of grasp stability via contact stiffness from contact mechanics insight," *Mechanism and Machine Theory*, vol. 134, pp. 625–644, 2019.

[38] L. Birglen, "Design of a partially-coupled self-adaptive robotic finger optimized for collaborative robots," *Autonomous Robots*, vol. 43, no. 2, pp. 523–538, 2019.

[39] J. Falco, K. Van Wyk, and E. Messina, "Performance metrics and test methods for robotic hands," *DRAFT NIST Special Publication*, vol. 1227, 2018.

[40] K. Kimble, K. Van Wyk, J. Falco, E. Messina, Y. Sun, M. Shibata, W. Uemura, and Y. Yokokohji, "Benchmarking protocols for evaluating small parts robotic assembly systems," *IEEE Robotics and Automation Letters*, vol. 5, no. 2, pp. 883–889, 2020.

[41] B. Rouzbeh, G. M. Bone, G. Ashby, and E. Li, "Design, implementation and control of an improved hybrid pneumatic-electric actuator for robot arms," *IEEE Access*, vol. 7, pp. 14 699–14 713, 2019.

BIOGRAPHY SECTION

Jérôme Bastien is currently pursuing a M.S. in Mechatronics at Ecole Polytechnique de Montréal, QC, Canada and a B.Eng. degree with Ecole Nationale d'Arts et Métiers, Paris, France. His research focuses on the study, optimization and design of compliant mechanisms.

Lionel Birglen received the B.Eng. degree in Mechatronics from Ecole Nationale Superieure des Arts et Industries de Strasbourg, Strasbourg, France, in 2000, and the Ph.D. degree in Mechanical Engineering from Universite Laval, QC, Canada. In 2005, he joined the Department of Mechanical Engineering, Polytechnique Montreal, QC. In 2013, he was a Visiting Associate Professor in the 3ME Department, TU Delft, Delft, The Netherlands and in 2018, a Visiting Full Professor at the Laboratoire d'Informatique, de Robotique et de Microelectronique de Montpellier (LIRMM), France. His research interests include the kinematic analysis and control of self-adaptive mechanisms, especially underactuated robotic hands. He is the Treasurer of the Canadian Committee for the Theory of Machines and Mechanisms, a Senior Member of the Institute of Electrical and Electronics Engineers, and a Member of the American Society of Mechanical Engineers, the Canadian Society of Mechanical Engineers, and the Canadian Aeronautics and Space Institute.